IOP Publishing Physics in Medicine and Biology

Phys. Med. Biol. **52** (2007) 2089–2106 doi:10.1088/0031-9155/52/8/004

A scatter-corrected list-mode reconstruction and a practical scatter/random approximation technique for dynamic PET imaging*

Ju-Chieh (Kevin) Cheng[1], Arman Rahmim[1,2], Stephan Blinder[3], Marie-Laure Camborde[3,4], Kelvin Raywood[3] and Vesna Sossi[1]

[1] Department of Physics and Astronomy, University of British Columbia, Vancouver, BC V6T 1Z1, Canada
[2] Department of Radiology, Johns Hopkins University School of Medicine, Baltimore, MD 21205, USA
[3] Pacific Parkinson's Research Centre, Vancouver, BC V6T 1Z1, Canada

E-mail: jcheng@phas.ubc.ca, vesna@phas.ubc.ca, arahmim1@jhmi.edu, blinder@phas.ubc.ca, marie@pet.ubc.ca and kelvin@pet.ubc.ca

Received 23 October 2006, in final form 31 January 2007
Published 26 March 2007
Online at stacks.iop.org/PMB/52/2089

Abstract

We describe an ordinary Poisson list-mode expectation maximization (OP-LMEM) algorithm with a sinogram-based scatter correction method based on the single scatter simulation (SSS) technique and a random correction method based on the variance-reduced delayed-coincidence technique. We also describe a practical approximate scatter and random-estimation approach for dynamic PET studies based on a time-averaged scatter and random estimate followed by scaling according to the global numbers of true coincidences and randoms for each temporal frame. The quantitative accuracy achieved using OP-LMEM was compared to that obtained using the histogram-mode 3D ordinary Poisson ordered subset expectation maximization (3D-OP) algorithm with similar scatter and random correction methods, and they showed excellent agreement. The accuracy of the approximated scatter and random estimates was tested by comparing time activity curves (TACs) as well as the spatial scatter distribution from dynamic non-human primate studies obtained from the conventional (frame-based) approach and those obtained from the approximate approach. An excellent agreement was found, and the time required for the calculation of scatter and random estimates in the dynamic studies became much less dependent on the number of frames (we achieved a nearly four times faster performance on the scatter and random estimates by applying the proposed method). The precision of the scatter fraction was

* This work was supported by the Canadian Institute of Health Research, a TRIUMF Life Science Grant, the Natural Sciences and Engineering Research Council of Canada UFA (V Sossi) and the Michael Smith Foundation for Health Research Scholarship (V Sossi).
[4] Present address: Radiation Oncology Victoria, 132 Grey Street, East Melbourne, 3002 VIC, Australia.

also demonstrated for the conventional and the approximate approach using phantom studies.

(Some figures in this article are in colour only in the electronic version)

1. Introduction

List-mode reconstruction for high-resolution PET imaging in which an increasing number of lines-of-response (LORs) are possible has been established to be particularly advantageous for studies with a low number of counts; data are reconstructed on an event-by-event basis thus rendering the reconstruction times proportional to the number of acquired events (Rahmim *et al* 2004b, Reader *et al* 2002). In contrast, conventional histogram-mode reconstruction has a fixed time cost for every frame since data are reconstructed on a line-of-response (LOR) basis. Histogram-mode reconstruction is thus timewise more efficient for studies with a large number of counts. As a result, especially in dynamic imaging, it would be practically advantageous to have the ability to choose the timewise optimal reconstruction mode for each frame on the basis of the number of events acquired during that temporal frame.

In this study, as elaborated in section 1, we have developed and investigated an ordinary Poisson list-mode expectation maximization algorithm (OP-LMEM) as built from previous work (Rahmim *et al* 2005) that includes a scatter correction based on the single scatter simulation (SSS) (Watson 2000). The implementation of this algorithm is discussed together with a comparison of images reconstructed with the corresponding sinogram-based algorithm (i.e. 3D ordinary Poisson ordered subset expectation maximization (3D-OP)) (Politte and Snyder 1991).

In dynamic imaging, the expected scatter and random events are generally estimated on a frame-by-frame basis. The justification for this approach is that the tracer distribution changes as a function of time, and therefore the scatter and random distributions will change accordingly. As a consequence, the time and storage requirements for the scatter and random estimates are proportional to the number of dynamic frames. Furthermore, given the often highly variable number of events per frame typical of dynamic scanning as shown in figure 1, the number of counts in the frame-based approach may not always be sufficiently high to produce an accurate scatter estimate (e.g. variation in the scatter fraction as will be addressed later). In this study, we examined an alternative practical approximate approach to the estimation of scatter and random events based on the observation that both scatter and random events have a very broad spatial distribution with very little high frequency content. In this approach, the scattered and random events are estimated using data averaged over several spatially similar temporal frames, and the scatter and random estimates for each individual temporal frame are then obtained by scaling the global estimate by the total number of true coincidences and random events in that frame respectively as elaborated in section 2. The main advantage of this method is a reduction in the time and data storage required to calculate and store the scatter and random estimates since the time and storage costs for the proposed method will be largely independent of the number of frames. An additional potential advantage might be achieved when the number of counts in a frame is low enough to introduce statistical variations in the frame-based scatter estimate provided the spatial tracer distribution changes minimally. The proposed method can be applied not only to the list-mode but also to the histogram-mode reconstruction. Methods and results are presented in sections 3 and 4 followed by discussion and concluding remarks in sections 5 and 6. All

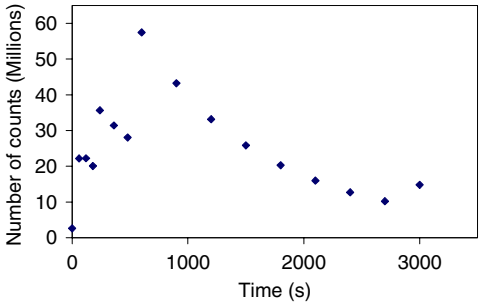

Figure 1. The number of counts within the frames for a typical ^{11}C dynamic study. Each point represents the number of counts acquired within a frame.

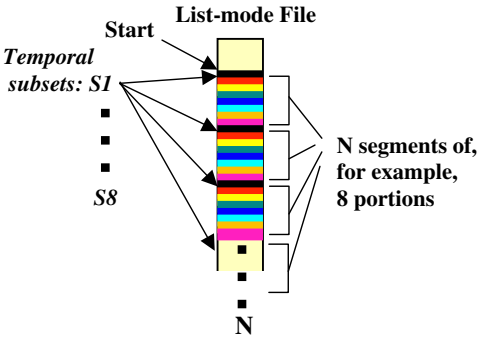

Figure 2. A dynamic frame is divided into a number of segments, with the segments further divided into, for example, eight portions (representing the number of subsets). The first list-mode subset S1 is then formed by regrouping the first portion from all the segments, as shown. This procedure is similarly repeated for subsequent subsets (S2, . . . , S8).

comparisons presented were performed with experimental data and were designed to test the performance of the scatter-corrected list-mode reconstruction (OP-LMEM) and the practical approximation in realistic scanning situations based on the practical uses of the reconstructed images, which are to obtain the time activity curves (TACs) and the binding potential (BP) values.

2. Ordinary Poisson EM in list-mode reconstruction

In subsetized histogram-mode reconstruction, the acquired data are divided into angular subsets in order to speed up the convergence of the reconstruction and reduce the number of iterations required (Hudson and Larkin 1994). On the other hand, in subsetized list-mode reconstruction, data acquired within a frame in the dynamic studies can be divided into temporal subsets (Reader *et al* 2002). In this work, the temporal subsets have been further 'segmented': they are now extracted from multiple segments in the list-mode data as depicted in figure 2 in order to minimize potential time-varying inconsistencies in the activity distributions across the sequential temporal subsets thus consistently iterating towards an average activity distribution within each dynamic frame (Rahmim *et al* 2005) (note: the data of a dynamic frame are the data acquired within the specified frame duration, the data of a 'segment' are a small part (short duration) of the dynamic frame and the data of a 'portion' are a small part of the segment).

The estimated image of any dynamic frame is therefore updated after processing through each regrouped temporal subset. The number of the segments we applied depends on the rate of variation of counts in the frame, i.e. it has been empirically found that when the number of counts changes rapidly within a single frame (as is usually the case during the first frame of dynamic scans) more segments need to be applied in order to minimize the variation of the number of counts (eventually resulting in image intensity) in between the subsets thus resulting in unbiased image updates between the subsets. For example, it has been found for our non-human primate studies that at least 30 segments need to be applied in the first dynamic frame and ten segments are sufficient for the rest of the frames.

The subsetized ordinary Poisson list-mode expectation maximization (OP-LMEM) algorithm is given by

$$\lambda_j^{m,l+1} = \frac{\lambda_j^{m,l}}{\sum_{i=1}^{I} w_{ii} g_{ij}} \sum_{k=1}^{N} g_{ikj} \frac{1}{\sum_{b=1}^{J} g_{ikb} \lambda_b^{m,l} + [\bar{r}_{ik} + \bar{s}_{ik}]/w_{ii}} \tag{1}$$

where $\bar{s}_{ik}$ are the expected mean scatter counts along the i_k^{th} LOR associated with the k^{th} event ($k = 1, \ldots, N$ where N is the total number of events). $\bar{r}_{ik}$ are the expected mean random counts along the i_k^{th} LOR associated with the k^{th} event. $\lambda_j^{m,l}$ is the image intensity (counts) in voxel j ($j = 1, \ldots, J$) at the m^{th} iteration and l^{th} subset. g_{ij} is the geometric probability of an emission from voxel j being detected along the i^{th} LOR. w_{ii} is the weight, assigned to each LOR, which accounts for sensitivity variations due to attenuation and normalization. The expected random estimate used in the OP-LMEM is computed and histogrammed separately for each frame. It is based on the variance-reduced delay coincidence technique in which crystal singles rates are estimated from the delayed-coincidence measurements (inherently including the effect of dead time), and then an iterative calculation of randoms rates is performed from the singles rate per crystal (Casey and Hoffman 1986, Badawi *et al* 1999, Byars *et al* 2005). The expected scatter estimate used in our OP-LMEM algorithm is based on a single scatter simulation (SSS) technique in which the scatter contributions are calculated and histogrammed into a scatter sinogram on a frame-by-frame basis (Watson 2000). This approach requires an intermediate histogramming step in the list-mode reconstruction to obtain the scatter and random estimates. It was originally thought that the scatter and random events should be estimated on a subset basis; however, in a single temporal subset the number of counts would be potentially too low to provide a reliable scatter and random estimates with the additional undesirable consequence that the time cost for estimating the scatter and random events would be proportional to the number of the list-mode subsets. As a result, a scatter and smoothed random sinogram is estimated for each frame (it will be addressed in section 2 that even the frame-based scatter and random estimates are still time consuming and may typically contain a low number of counts, and therefore a more practical scatter and random approximation technique is introduced).

In the OP-LMEM algorithm, the estimated scatter and random events are then scaled amongst the temporal subsets, taking into account different dead time and decay correction factors for the individual subsets, i.e. we note that unlike histogram-mode methods in which data subsets span the same time durations data subsets in list-mode reconstruction are temporally segmented and interleaved as shown in figure 2. For the particular example of the HRRT (high-resolution research tomograph, see section 3) scanner, in which scatter and random estimates are performed in 'span 3' (i.e. the LORs are axially compressed in a 2-to-1 and 1-to-1 pattern with a maximum ring difference of 67 and depth of interaction (DOI) rebinning thus giving ~450M LORs), the list-mode event coordinates were binned into the closest LOR in span 3 in order to use the corresponding scatter and random estimates, and the span 3-binned list-mode events were reconstructed to compare with the histogram-mode reconstruction in span 3.

Finally, we note that in order to speed up the convergence of OP-LMEM with the initial estimate of a uniform low activity image we introduce the scatter and random estimates into the image update factor only after the first subset. This is based on our finding that the image estimate quantitatively updates/scales itself much faster with the denominator of the OP-LMEM algorithm (equation (1)) not containing the scatter and random estimates in the first temporal subset of the first iteration. The image estimate obtained from the first subset will thus be more quantitatively commensurate with respect to the expected scatter and random estimates if obtained without the inclusion of the scatter and random estimates (i.e. less magnitude difference between the image, scatter and random estimates).

3. A practical scatter and random approximation technique

As previously mentioned, in order to speed up and increase the statistical quality in the scatter and random estimates, a practical scatter and random approximation technique was developed in this work. This technique is based on two observations:

- The scatter and random distributions are not very sensitive to the changes in the tracer distribution (i.e. the spatial scatter and random distributions are spatially much smoother compared to the distribution of the unscattered true events which correctly identifies the tracer distribution).
- The amount (magnitude) of scatter in each dynamic frame is proportional to the number of true coincidences (the pair of gamma rays originated from the same annihilation, i.e. the unscattered true events + the scattered events) in the frame, and likewise that of randoms is proportional to the global randoms counts in each frame.

In addition, the random estimate typically becomes less and less significant relative to the trues in the later frames of dynamic studies since the random fraction drops as the square of the activity thus increasing the 'tolerance' of the random estimate. By using a time-averaged scatter and random estimation followed by scaling the distribution according to the frame true coincidences and randoms, higher computational efficiency can be achieved. Furthermore, a potentially more precise scatter estimate can be obtained since it is derived from a data set with a higher number of counts when the spatial tracer distribution changes minimally.

After incorporating this approximation technique into the OP-LMEM algorithm (details of which are elaborated shortly), equation (1) becomes

$$\lambda_j^{m,l+1} = \frac{\lambda_j^{m,l}}{\sum_{i=1}^{I} w_{ii} g_{ij}} \sum_{k=1}^{N} g_{ikj} \frac{1}{\sum_{b=1}^{J} g_{ikb} \lambda_b^{m,l} + \left[\frac{C_{rf}}{C_{rt}} \bar{r}_{ik}^{A} + \frac{C_{tf}}{C_{tt}} \bar{s}_{ik}^{A} \right] \Big/ w_{ii}} \tag{2}$$

where C_{rf} is the number of random events (counts) in each individual frame, C_{rt} is the total number of random counts in the summed frame, C_{tf} is the number of true coincidences in each individual frame and C_{tt} is the total number of true coincidences in the summed frame. The true coincidences (which contain scatter) are obtained by subtracting the random counts from the total measured prompts for the given frame. $\bar{r}_{ik}^{A}$ is the random estimate for the summed frame (i.e. time-averaged estimate) and $\bar{s}_{ik}^{A}$ is the scatter estimate for the summed frame. In a similar fashion, this approximation can be incorporated into the 3D-OP algorithm.

This technique can be used reliably (as quantitatively demonstrated later) by using the plot of global true coincidence rate versus time, i.e. the dead time and decay corrected global time activity curve (TAC which can be easily obtained before data reconstruction), in order to guide the decision-making procedure as to which frames are to be grouped together for the scatter/random-estimation tasks. It has been indeed found empirically that whenever there is a large change (of slope) in the global TAC, there is generally a larger change in the spatial

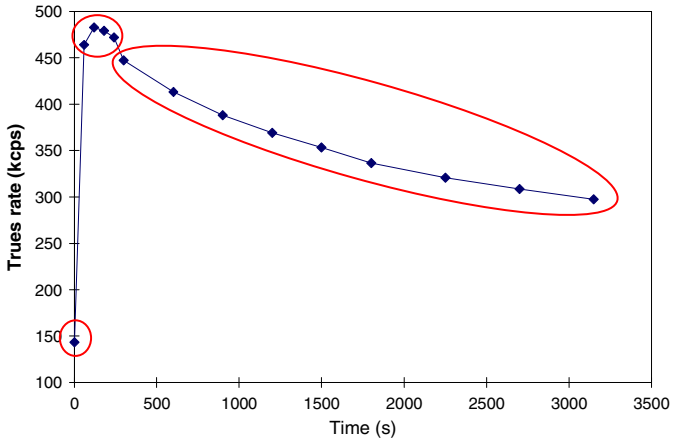

Figure 3. A global TAC for a ^{11}C-dihydrotetrabenazine dynamic non-human primate study. The solid line connects the measured data points and aids in determining larger changes in the true coincidence rate.

radioactivity distribution, and a separate scatter and random estimate needs to be performed for those frames.

Figure 3 shows a global TAC for a ^{11}C dynamic non-human primate study. Data from the frames grouped by the ellipses are summed to perform the average scatter and random estimates. Subsequent sections will demonstrate how this technique works on the real data obtained from tracers, which have a relatively rapid change of their spatial distribution at least during the first part of a dynamic scan, such as ^{11}C-dihydrotetrabenazine (DTBZ) and ^{11}C-raclopride (RAC). The difference in the spatial scatter distribution between the conventional and the approximate method will be examined using the conventional non-human primate study as the reference as will be discussed in the later sections. While the dynamic non-human primate study allows for a comparison between the scatter estimate obtained with the conventional method and the approximate one, it does not provide an absolute test of the precision or accuracy of the approximate method in a situation of a low number of acquired counts, which is the second potential advantage of the approximate method. This was addressed empirically with a phantom study (see phantom study 2), where the scatter fraction (SF) was first evaluated for a scan with a high number of counts ($\sim$55M) and subsequently for a series of data sets with $\sim$2M, $\sim$5M and $\sim$10M counts acquired at very similar count rates. The scan with a high number of counts was deemed to provide an essentially noise-free scatter estimate, while the variation of the SF estimates obtained from the data sets with a low number of counts was considered representative of the effects of statistical noise on the precision of the SF estimate since there was no change in the spatial tracer distribution in the phantom.

4. Methods

The following methods (acronyms) which will be described later in this section were tested and shown in the results section:

(a) Histogram-mode reconstruction with the conventional scatter and random estimation (3D-OP).

(b) List-mode reconstruction with the conventional scatter and random estimation (OP-LMEM).
(c) Filter backprojection of the conventional scatter estimation (FBP-S-conventional).
(d) Filter backprojection of the practical scatter approximation with one estimate from the entire scan (FBP-S-approx1e).
(e) Filter backprojection of the practical scatter approximation using the global TAC as guidance (FBP-S-approx).
(f) Histogram-mode reconstruction with the practical scatter and random approximation using the global TAC as guidance (3D-OP approx).
(g) List-mode reconstruction with the practical scatter and random approximation using the global TAC as guidance (OP-LMEM approx).
(h) 3D iterative OP reconstruction (both histogram and list modes) with the practical scatter and random approximation with one estimate from the entire scan (OP-approx1e).
(i) 3D iterative OP reconstruction (both histogram and list modes) with the practical scatter and random approximation using the global TAC as guidance (OP-approx).

Tomograph. Data were acquired on the second generation of the high-resolution research tomograph (HRRT) (Sossi 2005). This HRRT scanner has an octagonal detector ring design, with detector heads consisting of a double 10 mm layer of LSO/LYSO for a total of 119 808 detector crystals which corresponds to 4.5 billion possible LORs with no axial compression or 450 million LORs in span 3 with a sinogram data set size of 1.8 GB per frame for the scatter and random events and 0.9 GB per frame for the prompts (which includes the unscattered true, scatter and random events).

Phantom study 1. A 20 cm long, 10 cm radius phantom was used. The phantom has three 5 cm diameter cylindrical inserts, one of them was filled with water, another one was Teflon (two 'cold' inserts) and one with an initial ^{11}C radioactivity concentration of 47 kBq ml^{-1} ('hot' insert). The rest of the phantom was filled with an initial ^{11}C concentration of 11.7 kBq ml^{-1} ('background'), giving a hot to background ratio of 4.0. Twenty four dynamic frames (of 360 s each) were reconstructed. The measurement thus covered seven radioisotope half-lives, and the counts per frame ranged between 200M and 2M with the corresponding count rate between 555 and 5.5 kcps. This study was performed to evaluate the quantitative accuracy of the scatter-corrected list-mode reconstruction as compared to the conventional histogram-mode reconstruction (i.e. OP-LMEM versus 3D-OP).

Phantom study 2. A 30 cm long, 20 cm $\times$ 15 cm ellipse phantom was used. The phantom was filled uniformly with an initial ^{11}C radioactivity concentration of 7.73 kBq ml^{-1}. Data were grouped into sets of frames with similar numbers of counts to evaluate the reproducibility (precision) of the scatter fraction determination for both the conventional and the approximate scatter estimation; four frames with a very low number of counts ($\sim$2M counts), three frames with $\sim$5M counts and three frames with $\sim$10M counts in order. These numbers of counts were chosen since they are fairly representative of the number of counts encountered in human receptor imaging (see human study below). The count rate for these frames was approximately 4000 times higher than the intrinsic LSO true coincidence rate (intrinsic LSO true coincidence rate is about 100 cps) in order to exclude the effect of the intrinsic LSO background contribution to the scatter fraction. This study was performed to compare the robustness of the proposed approximate method and that of the conventional approach for situations where the number of acquired counts is low without changes in the spatial tracer distribution.

Non-human primate study. A non-human primate underwent a 60 min ^{11}C-dihydrotetrabenazine (DTBZ—a vesicular monoamine transporter VMAT2 marker) scan

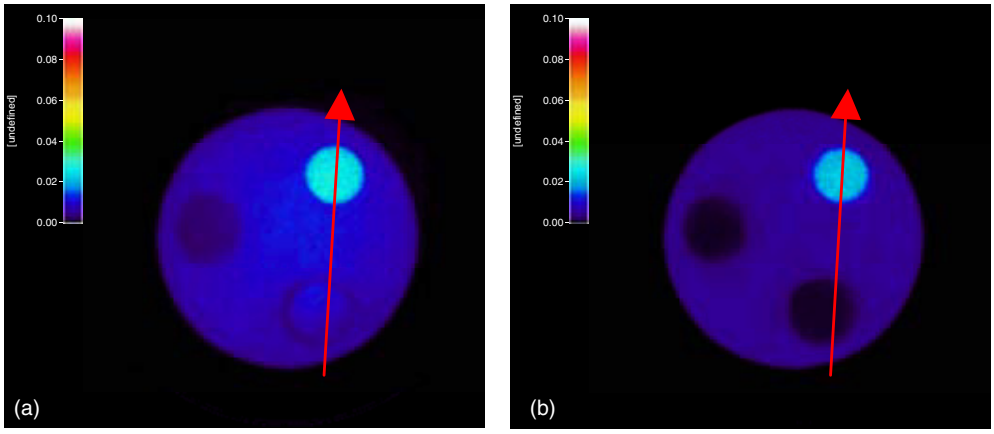

Figure 4. The transaxial (line) profile across the summed plane (a) without the scatter correction and (b) with the scatter correction.

on the HRRT (after a 6 min transmission scan and a 5 mCi bolus injection). Data were acquired in list mode and then framed into a 5 × 1 min, 5 × 5 min and 4 × 7.5 min framing sequence. The number of counts/frame in this study ranged from 140M to 13M and the count rate ranged between 600 and 50 kcps. The minimum number of counts per frame in this study (as in other non-human primate studies) was higher than the typical minimum number of counts in human studies. According to the results of the experiment described in the phantom study 2 (see results), the number of counts was always high enough to ensure a reproducible scatter fraction estimate by the conventional method. The conventional method was thus used as reference when evaluating the performance of the approximate method.

Human study. A human subject underwent a 60 min ^{11}C- raclopride (RAC—a D_2 receptor marker) scan on the HRRT (after a 6 min transmission scan and a 10 mCi Harvard pump injection). Data were acquired in list mode and then framed into a 4 × 1 min, 3 × 2 min, 8 × 5 min and 1 × 10 min framing sequence. The number of counts/frame in this study ranged from 57M to 2.6M and the count rate ranged between 370 and 25 kcps.

The dynamic studies were performed to validate both the quantitative accuracy of the scatter-corrected list-mode reconstruction and that of the practical scatter/random approximation method. The time and storage gained by applying the proposed approximate method will be discussed.

(1) *Comparison schemes for validating the scatter-corrected list-mode reconstruction.* Dynamic phantom images were reconstructed using (i) 3D-OP and (ii) OP-LMEM both with and without the scatter correction in span 3 and with a maximum ring difference of 67. The following comparisons were performed:

(1.1) *Transaxial profile comparisons (with and without the scatter correction).* A line profile was placed along a summed transaxial plane (summed over 100 axial planes). The summation was performed so as to minimize the contribution of statistical errors and emphasize the potential presence of systematic differences. The line traverses the hot spot and one of the cold spots (Teflon) as shown in figure 4. The transaxial profiles of all 24 frames were compared between the histogram- and list-mode reconstructions with the same number of subsets and iterations (four iterations with eight subsets). In addition, another profile was arbitrarily placed on a single plane to check the statistical variations between the reconstructions.

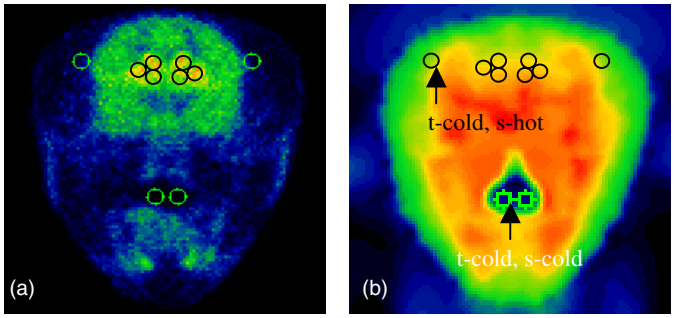

Figure 5. ROIs for the selected hot and cold spots in the striatum plane placed (a) in the emission image and (b) in the scatter image which is obtained by reconstructing the scatter events using the filter backprojection.

(1.2) *Axial profile comparisons (with the scatter correction).* Mean voxel intensities within each axial plane were plotted as a function of the axial position. The placed ROI covered the entire cross section of the phantom (i.e. including the hot, cold and background regions). The axial profiles of all frames were compared between the histogram- and list-mode reconstructions.

(1.3) *Contrast, ROI and voxel noise versus number of iterations comparisons (with the scatter correction).* The per cent contrast of the cold cylinder (i.e. [1-mean ROI activity of the cold spot over that of the average background] $\times$ 100%) and the coefficient of variation (for both ROI level and voxel level) of the background were calculated for all frames according to the NEMA protocol (National Electrical Manufacturers Association 2001) as a function of the number of iterations for the OP-LMEM and the 3D-OP reconstructions. Contrast and noise were plotted as a function of number of iterations, and comparison was performed between histogram- and list-mode reconstructions both with and without a 2 mm 3D Gaussian filter.

(1.4) *Time activity curve (TAC) comparisons (with the scatter correction).* The TAC, with the ROI described in (1.2) which covers the entire cross section of the phantom (i.e. including the hot, cold and background regions) on a single plane, was plotted over all frames for 3D-OP and OP-LMEM reconstructions for the phantom, non-human primate (figure 5) and human studies with decay and dead time corrections.

(1.5) *Binding potential (BP) comparisons (with the scatter correction).* The binding potential for the non-human primate study was computed using the tissue input Logan graphical approach (Logan *et al* 1996) using the cerebellum as reference region for 3D-OP and OP-LMEM reconstructions.

(1.6) *Reconstruction time cost comparisons (with the scatter correction):* The reconstruction time cost was plotted as a function of the number of counts in each frame for both 3D-OP and OP-LMEM reconstructions. In all cases, the same number of computer processors (Dual Xeon 2.8 GHz blade processors with 2.5 GB RAM and gigabit Ethernet networking with jumbo-frame option) was used. The time costs for the rebinning process and estimating the scatter and random corrections are excluded in the comparison since they are the same for both 3D-OP and OP-LMEM.

(2) *Comparison schemes for validating the practical scatter/random approximation technique.* The quantitative accuracy of this technique was checked on three levels. First, the global scatter

fractions of phantom studies (no change in the spatial tracer distribution) were computed for the conventional and the approximate methods. On a second level, the spatial scatter (randoms) distribution and TACs themselves were compared between the conventional and the approximate method using the non-human primate data (with rapidly varying spatial tracer distribution). Since the estimated scatter and random sinograms contain many segments (direct and oblique planes), it is not very efficient to compare the sinograms directly. As a result, estimated scatter and smoothed random events were reconstructed using FBP (filtered backprojection: fast and linear) for each frame separately (i.e. the conventional method), for a summed frame with the entire scan duration (i.e. the approximate method with only one estimate) and for a number of summed frames determined according to the behaviour of the global count rate curve (i.e. the approximate method with three estimates, see figure 3) followed by scaling according to the global number of true coincidences or randoms in each frame. On a third level, the effect of the approximate scatter and random correction on the quantitative accuracy of the final images was investigated by reconstructing the emission data using 3D iterative OP algorithm (both histogram mode and list mode) in span 3 for the non-human primate and human studies for both the conventional and approximate scatter/random estimations. The following comparisons were performed:

(2.1) *Scatter fraction comparisons*. The scatter estimate for the second phantom study was computed for each frame separately (conventional) with the selected number of counts and count rate as mentioned previously, and the scatter estimate was computed for a summed frame with the total duration of all the separate frames followed by scaling according to the number of true coincidences in each frame (approximate method). The scatter fraction of the phantom was then calculated by dividing the total number of counts from the scatter estimate by that of the true coincidences (i.e. unscattered trues + scatter or prompt − random) for each frame and compared between the one obtained from the conventional and that obtained from the approximate method. The scatter fraction estimate obtained from the entire data set was considered a noise-free evaluation of the scatter fraction and was used as reference when comparing the scatter fraction values obtained from the individual low statistics frames.

(2.2) *Spatial scatter distribution comparisons*. For the non-human primate study, the reconstructed scatter images obtained from the approximate method were subtracted from the ones obtained using the conventional method (reference images), and the difference was then divided by the reference images. This relative spatial difference was examined visually. A radial profile was also placed at the plane with the greatest difference in the scatter images between the conventional and the approximate method.

(2.3) *Time activity curve (TAC) comparisons*. The time activity curves, with the ROIs (as shown in figure 5) in the striatum (right/left caudate, putamen and ventral striatum), cerebellum and a number of selected cold regions, were plotted over 14 frames of the non-human primate scan for the scatter, random and the emission (unscattered trues) images without the decay and dead time corrections. Two kinds of cold spots are defined here: one is defined (t-cold, s-hot) as the cold spot in the unscattered trues image with a corresponding hot spot in the scatter image, i.e. higher density region with no or very low radioactivity, for example bones for most tracers. The other one (t-cold, s-cold) is defined as the cold spot in the unscattered trues image with a corresponding cold spot in the scatter image, i.e. lower density region with very low or no radioactivity such as air and water as shown in figure 5(b). Those two kinds of cold spots were introduced to check the limit of the approximate method since the radioactivity estimated in the cold spots is sensitive to small changes in the scatter estimate. The TACs were then compared between the images reconstructed using the conventional and the approximate methods by

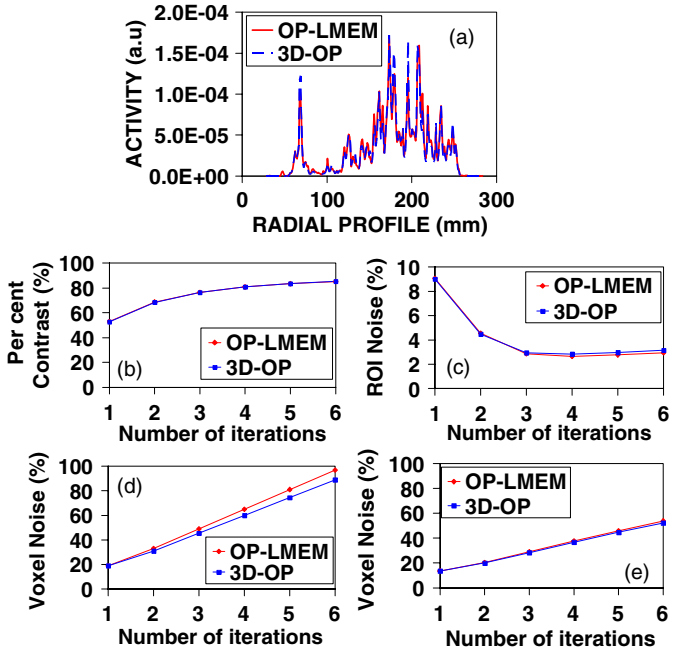

Figure 6. (a) Transaxial profile comparison on a single plane (∼15M counts), (b) contrast versus number of iteration comparison, (c) ROI noise versus number of iteration comparison; there is virtually complete overlap between the results obtained with the two algorithms, (d) voxel noise versus number of iteration comparison and (e) voxel noise versus number of iteration comparison after applying a 2 mm 3D Gaussian filter.

estimating the ratio of their values relative to each frame (i.e. $\mathrm{ROI}_{\mathrm{approximate}}/\mathrm{ROI}_{\mathrm{conventional}}$ for each frame). In addition, the same TAC analysis was also performed in voxel level for the emission images, and the voxel-based ratio was calculated between the approximate and the conventional method (similar to the ROI ratio defined above).

(2.4) *Binding potential (BP) comparisons.* As described in (1.5), the binding potentials as obtained from the images reconstructed with the conventional and the approximate method were also compared.

5. Results

Profile comparisons (1.1), (1.2) between OP-LMEM and 3D-OP. In all cases, the transaxial and axial profiles obtained with 3D-OP and OP-LMEM virtually overlap for all frames of the phantom study. However, when examining the transaxial profiles on a single plane, it has been observed that there are some minor statistical variations between images reconstructed using 3D-OP and OP-LMEM when the number of counts within the frame is lower than 25M as shown in figure 6(a); the cause of this variation will be discussed in section 5.

Contrast and noise comparisons (1.3) between OP-LMEM and 3D-OP. The per cent contrast, ROI noise and voxel noise versus number of iterations comparisons for frame 10 are shown in figures 6(b)–(e), respectively. Frame 10 was arbitrarily chosen here, and other frames all show similar results.

Table 1. The quantitative binding potential values for 3D-OP and OP-LMEM obtained with the conventional and the practical scatter/random approximation for the non-human primate study.

	3D-OP	3D-OP approx	OP-LMEM	OP-LMEM approx
Right caudate	2.70	2.70	2.77	2.78
Left caudate	2.93	2.92	2.89	2.90
Right putamen	3.07	3.07	3.16	3.17
Left putamen	3.01	3.01	3.01	3.01
Right-ventral striatum	2.42	2.42	2.40	2.40
Left-ventral striatum	2.55	2.55	2.49	2.49

Here, the contrast also agrees between histogram- and list-mode reconstructions. In addition, the ROI noise comparison shows a good agreement between the two algorithms. The voxel noise however shows a slight difference between 3D-OP and OP-LMEM as depicted in figure 6(d), which is likely due to the difference between a voxel-driven backprojection (3D-OP) and a LOR-driven backprojection (OP-LMEM): for the voxel-driven backprojection a voxel can get contributions from millions of LORs, whereas for the LOR-driven backprojection a LOR can only contribute to a few voxels. As shown in figure 6(e), after applying a 2 mm 3D Gaussian filter, which is commonly used when reconstructing HRRT data, the voxel noise for the 3D-OP reconstruction agrees very closely with that for the OP-LMEM reconstruction thus minimizing the practical difference between the images reconstructed using each algorithm.

Accuracy of TAC comparisons (1.4) between OP-LMEM and 3D-OP. The TAC analysis showed very good agreement between results obtained with the histogram-mode and list-mode reconstructions for the phantom study (i.e. the differences in the ROI values are within ∼2% with respect to the 3D-OP ROI value). A representative TAC comparison for the non-human primate study (where the counts per frame vary from 140M to 13M) between 3D-OP and OP-LMEM is shown in figure 7(a). The TACs agree within ∼5%, and the difference is expected to be due to the aforementioned statistical variation between 3D-OP and OP-LMEM (see figure 6(a)). Similar results were also obtained from the human studies.

Binding potential (BP) comparisons (1.5) between OP-LMEM and 3D-OP. In all cases examined, we found at most a ∼3% difference in the BP estimated when comparing analyses performed on data reconstructed with 3D-OP and OP-LMEM. The quantitative binding potential values of a representative study for each algorithm are shown in table 1.

Reconstruction time cost comparisons (1.6) between OP-LMEM and 3D-OP. The reconstruction time cost as a function of number of counts is depicted in figure 7(b). The intercept between the two curves shown in figure 7(b) determines the threshold value for the dual reconstruction scheme (which will be discussed in section 5), and in this case a threshold value of 50M counts was obtained, i.e., with our current implementation of the list-mode reconstruction, OP-LMEM is more efficient than 3D-OP when the number of counts within the frame is less than 50M.

Scatter fraction comparisons (2.1) between the conventional and the approximate scatter correction method. The reference scatter fraction of 39.76% was obtained from the entire data set. The scatter fraction comparisons are shown in figure 8. As shown in figure 8, the scatter fraction obtained from the approximate method is more consistent than that obtained from the conventional method since (1) the approximated scatter estimate is scaled according to the frame true coincidences thus ensuring a consistent scatter fraction for each frame and

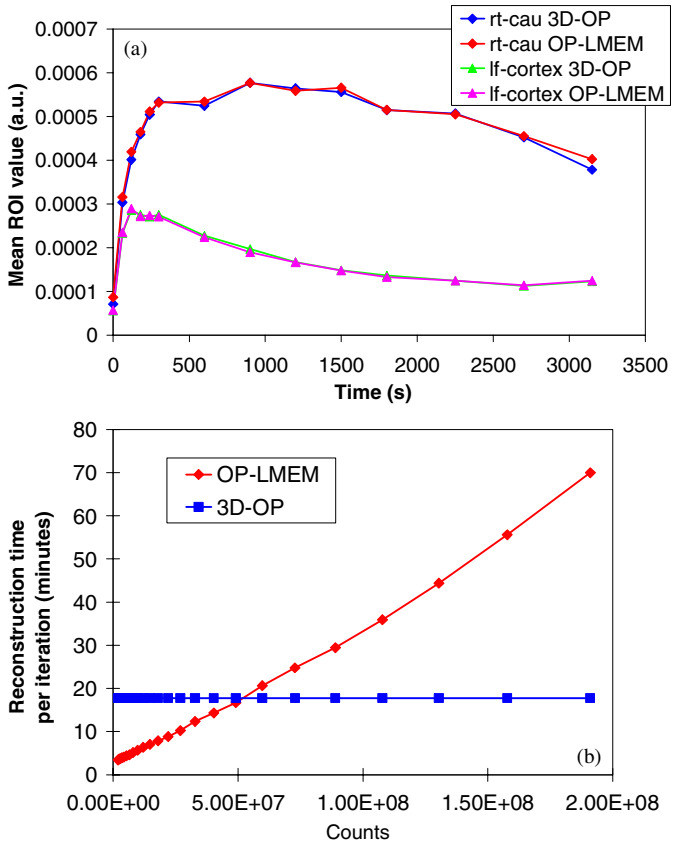

Figure 7. (a) TAC comparison between 3D-OP and OP-LMEM for the non-human primate study; the TACs for the right-caudate (rt-cau) and the left-cortex (lf-cortex) regions are shown here and (b) the reconstruction time cost versus the number of counts using the same number of processors for both 3D-OP and OP-LMEM reconstructions.

(2) a sufficiently high number of counts are used in the approximated scatter estimate, whereas a low number of counts used in the conventional frame-based estimate is likely to result in a variation of scatter tail-fitting used in the SSS technique. As expected, the variation of the scatter fraction decreases as the number of counts increases for both methods.

Spatial scatter distribution comparisons (2.2). The relative difference in the spatial scatter distribution between the approximate (with three estimates) and the conventional (used as the reference as discussed previously) method was first examined visually. Large differences were only observable outside the image of the object. When limiting the comparison to the actual image of object, a maximum difference or spatial inaccuracy of approximately 10% was observed as shown in figure 9. The contribution of this difference to the TAC analysis will be addressed shortly.

Scatter and random TAC comparisons (2.3) between the conventional and the approximate scatter and random correction method. The TAC and ratio of TAC comparisons of the ROIs placed on the scatter images for the non-human primate study are shown in figures 10 and 11.

Hot spots. As shown in figure 10 with the corresponding TAC ratio shown in figure 11(a), the scatter TAC of the conventional method agrees with the approximate method (one estimate,

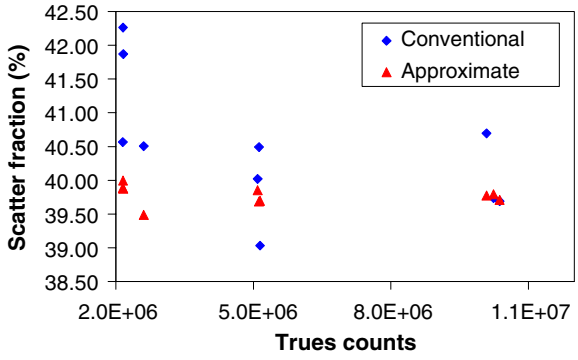

Figure 8. The scatter fraction comparisons between the conventional and the approximate method for frames with similarly low number of counts (∼2M, ∼5M and ∼10M) at a similar count rate (∼4000 times higher than the LSO background true coincidence rate).

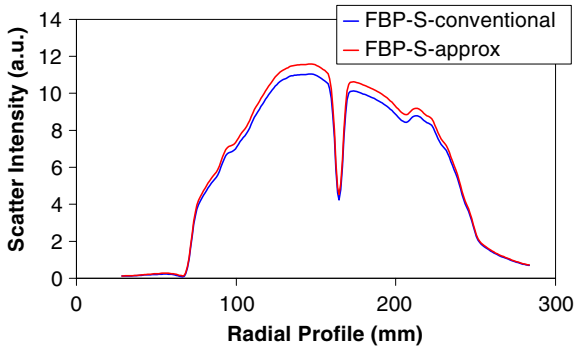

Figure 9. The radial profile comparison in the scatter images of the non-human primate study between the conventional (FBP-S-conventional) and the approximate method with three estimates obtained using the global TAC as guidance (FBP-S-approx) in the plane with the greatest observed difference.

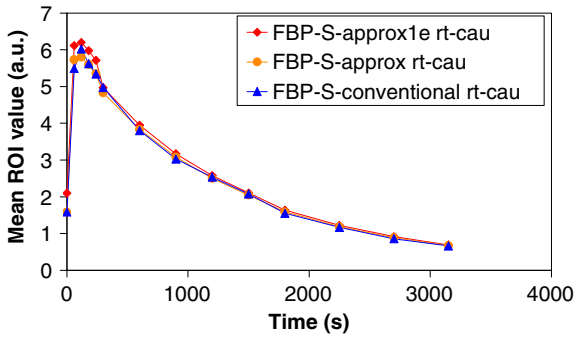

Figure 10. The scatter TAC (without decay and dead time corrections) comparison for the right-caudate region of the non-human primate study between the conventional (FBP-S-conventional) and the approximate method with one (FBP-S-approx1e) and three estimates obtained using the global TAC as guidance (FBP-S-approx).

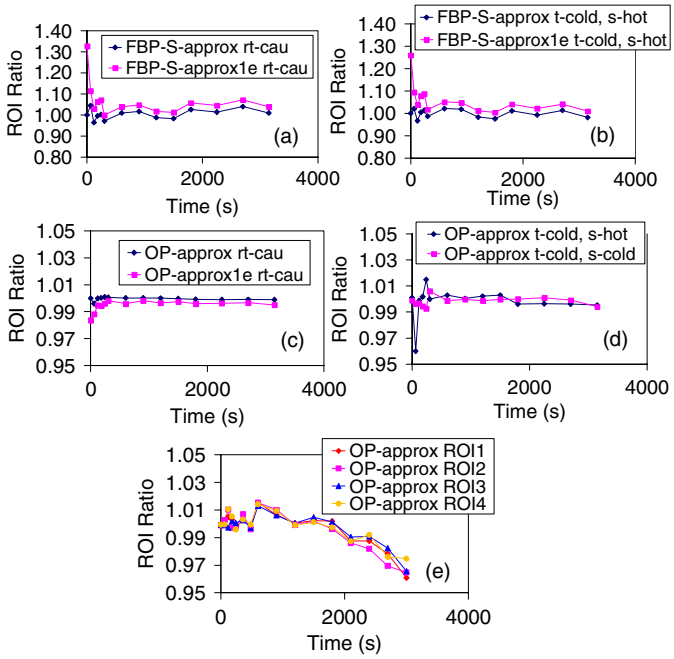

Figure 11. (a) The ratio of the scatter TAC comparisons for the right-caudate region of the non-human primate study between the conventional and the approximate method with one (FBP-S-approx1e) and three estimates obtained using the global TAC as guidance (FBP-S-approx), (b) the ratio of the scatter TAC comparisons for the selected cold spots as shown in figure 5 which contain low radioactivity but correspond to higher density regions, (c) the ratio of the TAC comparisons for the right-caudate region of the non-human primate study between the conventional and the approximate method with one (OP-approx1e) and three estimates obtained using the global TAC as guidance (OP-approx), (d) the ratio of the TAC comparisons for the selected cold spots as shown in figure 5 with three estimates and (e) the ratio of the TAC comparisons of the four striatum ROI regions of the human study between the conventional and the approximate method with four estimates (according to the global TAC rebinning scheme).

i.e. FBP-S-approx1e) within 10% except for the first frame which is during the uptake period where there was a significant change in the tracer distribution. The ratio of the TAC basically shows the variation in the distribution between the frame-based estimate and the time-averaged estimate. Figure 11(a) also demonstrates the improvement achieved with the approximate method using the global TAC as guidance (FBP-S-approx) according to the rebinning scheme described in section 2 (figure 3), i.e. the conventional and approximate methods agree within 5% for all frames. The TAC for the right caudate was arbitrarily chosen, and similar results were obtained from all other ROIs. The same analysis for the smoothed random images was performed, and the conventional method agrees with the approximate method within 5% for both one and three estimates; the (up to) 5% difference was only observed in the last three frames where the random fraction is lower than 15%.

Cold spots. As shown in figure 11(b), the approximate method works quite well in the t-cold, s-hot regions, while somewhat higher variation was observed for t-cold, s-cold regions. Again, significant improvement achieved using the global TAC as guidance is shown for the cold spots. Very similar results were obtained for the smoothed random TAC in the selected cold spots as well.

TAC comparisons (2.3) between the conventional and the approximate scatter and random correction method (non-human primate and human subject). The ratio of the TAC comparisons between the conventional and the approximate method with one and three estimates (using the global TAC as guidance) for the non-human primate study is shown in figure 11(c). The net contribution from the difference in the scatter (as mentioned in the spatial scatter distribution comparison (2.2)) and random estimates between the conventional and the approximate method with one estimate (the worst case scenario) is shown to be less than 3% in the TAC as depicted in figure 11(c). The improvement achieved with three estimates is also shown: the TAC using the approximate method with three estimates agrees with that using the conventional method within 1%. The same analysis has also been done for the selected cold spots, and the TAC using the approximate method (three estimates) agrees with that using the conventional method within 4% as shown in figure 11(d). Here, a better ROI ratio was obtained for the t-cold, s-cold spot (very low activity) as compared to that of the t-cold, s-hot spot since the scatter fraction for the t-cold, s-cold spot is much lower than that of the t-cold, s-hot spot; thus, the scatter estimate contributes much less to the emission image for the t-cold, s-cold spot. The ratio of the voxel TAC comparison also showed similar and consistent results; the voxel TAC using the approximate method with three estimates agrees with that using the conventional method within 1% for the hot voxels and within 4% for the cold voxels in the object. The ratio of the TAC comparison for the human study is shown in figure 11(e) (without motion correction). Here, up to a 5% variation in the TAC between the conventional and the approximate method has been observed. In this case, it is however harder to interpret the meaning of the difference between the methods since patient motion does affect the alignment between the transmission and emission scans, which would by itself affect the accuracy of the scatter correction. Moreover, part of the difference is expected to be due to the variation of scatter fraction for frames with a low number of counts using the conventional method since the last few frames of the human study contain less than ∼10M counts. A more meaningful comparison should be made after patient motion correction is implemented (Rahmim *et al* 2004a).

Binding potential (BP) comparisons (2.4) between the conventional and the approximate scatter and random correction method (non-human primate). The BP analysis also showed an excellent agreement (within ∼0.2%) between the conventional and the approximate method (using the global TAC as guidance) as shown in table 1. Both histogram-mode and list-mode reconstructions show the same agreement between the conventional and the approximate method.

6. Discussion

A very good agreement between 3D-OP and OP-LMEM was obtained for most figures of merit examined; only statistical variations were observed when the number of counts within the frame was lower than 25M. These variations were attributed to the fact that although the two methods use the same overall data the subsets are not identical (i.e. the difference between the histogram-mode spatial angular subsets and the list-mode temporal subsets): in a situation of low counts, statistical differences in the subsets will produce a different reconstructed image, and up to a 5% difference has been observed in the examined ROI values and at most a 3% in the binding potential values calculated with TACs obtained from images reconstructed with the two algorithms. Considering the scan-to-scan BP estimate variability is approximately 10% for most methods, a 3% difference due to the reconstruction algorithm is considered acceptable.

With regard to the practical scatter/random approximation technique, in a situation of a low number of counts per frame a more consistent scatter fraction was obtained from the approximate method due to the higher number of counts used in the scatter calculation (in both estimating the spatial scatter distribution and tail-fitting to the scatter tail of the measured true coincidences) and the scaling according to the frame true coincidences. For the non-human primate studies in which no motion was present and there is a sufficient number of counts within each frame to obtain a consistent scatter fraction for the conventional method (i.e. good as an absolute reference), a very good agreement in the spatial scatter distribution and TAC comparisons between the conventional and the approximate method was obtained. On the other hand, for human studies the frame-based estimate is not very accurate since it is sensitive to both patient motion and the number of events (i.e. the number of counts in each frame for the human studies ranges from 57M to 2.6M which is about two to three times lower than that for the non-human primate studies) in the frame thus possibly producing somewhat inaccurate results, and therefore it cannot be used as the absolute reference. A fully motion-corrected analysis would therefore likely further demonstrate the validity of the approximate method in the human studies for tracers with rapidly varying spatial distribution. For tracers with relatively uniform spatial distribution and phantom studies, the approximate method is expected to be more accurate than the conventional method due to the higher statistical quality of the data used in the scatter and random estimates as demonstrated in comparison (2.1). Furthermore, the time and storage costs for scatter and random estimates in the dynamic studies became largely independent of the number of frames by applying the proposed method. We achieved a nearly four times reduction in computational demands (both time and storage) related to the scatter and random estimates for the studies presented here (i.e. calculating three estimates instead of 14 as depicted in figure 3).

Since very similar quantitative accuracy between the list-mode and the histogram-mode reconstruction has been achieved and the practical scatter/random approximation technique can be applied to both list-mode and histogram-mode reconstructions, a dual (histogram/list-mode) reconstruction scheme is currently being developed to reduce the time cost for dynamic PET imaging using the HRRT scanner which often has a high number of LORs/number of counts ratio. The criteria which determine the switching point of reconstruction mode should be addressed. One criterion we are currently considering is the number of coincidence events or the size of the data file. For the case of our HRRT scanner, there are 450M LORs in span 3; therefore, ideally if the number of events in a dynamic frame is less than the number of LORs (a threshold value of 450M), then one should use the event-based list-mode reconstruction and vice versa given that both reconstruction algorithms are equally optimized. The intercept between the two curves shown in figure 7(b) determines the threshold value for the dual reconstruction scheme, but in this case a threshold value of 50M counts was obtained since our OP-LMEM is not fully optimized as compared to 3D-OP.

7. Conclusion

Results from phantom and non-human primate studies look excellent from the above comparisons. In particular, the excellent agreement reached between OP-LMEM and 3D-OP indicates that the implementation of this scatter correction method into the list-mode algorithm is appropriate thus reaching the same level of quantification accuracy as 3D-OP. At present with 3D-OP being fully optimized for speed, while this is not yet the case for our OP-LMEM, we have found that for frames with less than 50M counts OP-LMEM is more advantageous timewise, and that might indicate the threshold value for an eventual dual reconstruction scheme to be 50M. In addition, a practical scatter/random approximation technique has also

shown to be efficient and accurate (i.e. time and storage costs are largely independent of the number of dynamic frames).

In conclusion, we have developed an efficient OP-LMEM algorithm which produces images virtually identical to those obtained with the histogram-mode counter part and a practical scatter/random approximation technique which is applicable to both list-mode and histogram-mode reconstructions. These studies contribute to decreasing the computational burden for high-resolution quantitative imaging and indicate feasibility for a future development of a dual (histogram/list-mode) reconstruction scheme for dynamic PET imaging.

Acknowledgment

The authors would especially like to thank Dr Doris Doudet for providing the non-human primate data.

References

Badawi R D, Miller M P, Bailey D L and Marsden P K 1999 Randoms variance-reduction in 3D-PET *Phys. Med. Biol.* **44** 941–54

Byars L G, Sibomana M, Burbar Z, Jones J, Panin V, Barker W C, Liow J-S, Carson R E and Michel C 2005 Variance reduction on randoms from delayed coincidence histograms for the HRRT *IEEE Med. Imaging Conf. Rec. (23–29 Oct. 2005)* vol 4 pp 2622–6

Casey M E and Hoffman E J 1986 Quantitation in positron emission tomography: 7. A technique to reduce noise in accidental coincidence measurements and coincidence efficiency calibration *J. Comput. Assist. Tomogr.* **10** 845–50

Hudson H M and Larkin R S 1994 Accelerated image reconstruction using ordered subsets of projection data *IEEE Trans. Med. Imaging* **13** 601–9

Logan J, Fowler J S, Volkow N D, Wang G J, Ding Y S and Alexoff D L 1996 Distribution volume ratios without blood sampling from graphical analysis of PET data *J. Cereb. Blood Flow Metab.* **16** 834–40

National Electrical Manufacturers Association 2001 *NEMA Standards Publication NU 2-2001: Performance Measurements of Positron Emission Tomographs*

Politte D G and Snyder D L 1991 Corrections for accidental coincidences and attenuation in maximum-likelihood image reconstruction for positron-emission tomography *IEEE Trans. Med. Imaging* **10** 82–9

Rahmim A, Bloomfield P, Houle S, Lenox M, Michel C, Buckley K R, Ruth T J and Sossi V 2004a Motion compensation in histogram-mode and list-mode EM reconstructions: beyond the event-driven approach *IEEE Trans. Nucl. Sci.* **51** 2588–96

Rahmim A, Cheng J-C, Blinder S, Camborde M-L and Sossi V 2005 Statistical dynamic image reconstruction in state-of-the-art high resolution PET *Phys. Med. Biol.* **50** 4887–912

Rahmim A, Lenox M, Reader A J, Michel C, Burbar Z, Ruth T J and Sossi V 2004b Statistical list-mode image reconstruction for the high resolution research tomography *Phys. Med. Biol.* **49** 4239–58

Reader A J, Ally S, Bakatselos F, Manavaki R, Walledge R, Jeavons A P, Julyan P J, Zhao S, Hastings D L and Zweit J 2002 One-pass list-mode EM algorithm for high-resolution 3-D PET image reconstruction into large arrays *IEEE Trans. Nucl. Sci.* **49** 693–9

Sossi V *et al* 2005 The second generation HRRT—a multi-centre scanner performance investigation *IEEE Med. Imaging Conf. Rec. (23–29 Oct. 2005)* vol 4 pp 2195–9

Watson C C 2000 New, faster, image-based scatter correction for 3D PET *IEEE Trans. Nucl. Sci.* **47** 1587–94